Journal of Materials Chemistry C

ROYAL SOCIETY OF CHEMISTRY

COMMUNICATION

View Article Online
View Journal

Check for updates

Cite this: DOI: 10.1039/d3tc03904h

Received 25th October 2023,
Accepted 18th December 2023

DOI: 10.1039/d3tc03904h

rsc.li/materials-c

Published on 18 December 2023. Downloaded by Universiteit Twente on 1/16/2024 1:54:30 PM.

Achieving low energy consuming bio-based piezoelectric nanogenerators *via* modulating the inner layer thickness for a highly sensitive pedometer†

Zixiong Sun, *[abcde] Siting Wang,[a] Shibo Zhao,[a] Hansong Wei,[b] Guodong Shen, *[f] Yongping Pu[g] and Sufeng Zhang*[b]

Considering their drawbacks of environmental pollution, biodegradable cellulose-based materials are becoming one of the most promising alternative candidates for conventional petroleum-based polymers, which are considered the fundamental materials for dynamical units in human–machine interaction systems. Using an up-to-date hydrogen bond replacement strategy, which means using the highly electronegative F^- in polyvinylidene fluoride (PVDF) to replace the intramolecular hydrogen bonds in cellulose for weakening the self-assembly behavior, herein, multilayer-structured piezoelectric nanogenerators (PENGs) composed of cellulose, a small amount of PVDF, and $Ba_{0.7}Ca_{0.3}Zr_{0.2}Ti_{0.8}O_3$ (BCZT) fillers were fabricated *via* modified tape-casting technology. Due to the hydrogen bond network, which was confirmed using multiple characterization methods, the fillers dispersed uniformly in the matrix. Through changing the inner layer thickness, the output performance of the PENGs can be subtly modulated, which is revealed to be caused by the synergistic effect between the trapped electrons and the inter-squeezing between adjacent particles by employing the band theory. When applied to a pedometer, one of the essential devices for monitoring human health, such a modulation can significantly improve its sensitivity. The water contact angle test also indicates their potential for use in humid environments. Compared with some typical cellulose-based PENGs, our device shows outstanding performance in P_D/F, defined as the power density triggered by unit force, indicating our PENG's low energy consumption characteristic.

As human society enters the era of Industry 4.0 (the fourth industrial revolution), significant development has been achieved in flexible electronics that are being integrated into human–machine interaction systems. Considering the energy crisis at the same time, the requirements for such devices at this time have to be high biocompatibility, biodegradability, and excellent mechanical properties, which enable them to be applied in limited space.[1–4] Petroleum-based dielectric polymers have been used for a long time in flexible devices for their optimistic performance, while their degradation process brings the drawbacks of severe environmental pollution.[5,6] Among all candidates, cellulose-based polymers have great potential to meet all three requirements mentioned above for their abundant reserves and good intrinsic polarization. Most commonly used materials in artificial intelligence-based sensors are usually functionalized for storing and converting energy. In the energy storage field, the energy storage density (ESD) of cellulose-based dielectric films has been increased from 5.7 J cm^{-3} to 27.3 J cm^{-3} *via* morphological control, interface modification, and so on.[7–13] As to the field of energy conversation or harvesting, numerous studies on piezoelectric nanogenerators (PENGs) have been reported due to their vast application prospects. Using the *in situ* synthesis method, micro-flower-like vanadium-doped ZnO was uniformly dispersed in a bacterial cellulose matrix, and a power density (P_D) of 0.06 μW cm^{-2} was achieved.[14] When changing the matrix material to regenerated cellulose, a higher power density of 0.19 μW cm^{-2} was obtained in 2,2,6,6-tetramethylpiperidine-1-oxyl-oxidized cellulose nanofibril/molybdenum disulfide

[a] School of Electronic Information and Artificial Intelligence, Shaanxi University of Science and Technology, Xi'an 710021, P. R. China. E-mail: SunZX@sust.edu.cn
[b] Shaanxi Provincial Key Laboratory of Papermaking Technology and Specialty Paper Development, National Demonstration Center for Experimental Light Chemistry Engineering Education, Key Laboratory of Paper Based Functional Materials of China National Light Industry, Shaanxi University of Science and Technology, Xi'an, 710021, P. R. China. E-mail: zhangsufeng@sust.edu.cn
[c] Key Laboratory of Auxiliary Chemistry and Technology for Chemical Industry, Ministry of Education, Shaanxi University of Science and Technology, Xi'an 710021, P. R. China
[d] Shaanxi Collaborative Innovation Center of Industrial Auxiliary Chemistry and Technology, Shaanxi University of Science and Technology, Xi'an 710021, China
[e] MESA+ Institute for Nanotechnology, University of Twente PO Box 217, 7522 NH Enschede, The Netherlands
[f] School of Textile Science and Engineering, Xi'an Polytechnic University, China. E-mail: shenguodong@xpu.edu.cn
[g] School of Materials Science and Engineering, Shaanxi University of Science and Technology, Xi'an 710021, P. R. China

† Electronic supplementary information (ESI) available. See DOI: https://doi.org/10.1039/d3tc03904h

Published on 18 December 2023. Downloaded by Universiteit Twente on 1/16/2024 1:54:30 PM.

nanosheet bio-nano composite piezoelectric films.[15] This power density was further enhanced to 0.19 μW cm^{-2} after adding $BaTiO_3$ particles. Compared to a dense matrix, a cellulose aerogel film, which contains abundant mesopores with high porosity and specific surface area, performs much better. A 1.29 μW cm^{-2} P_D was reached in freeze-drying-prepared 2,2,6-tetramethylpiperidine 1-oxyl-oxidized cellulose aerogel films.[16] In X. Huang's work, a similar technology was used. A P_D of 2.95 μW cm^{-2} was obtained using a cellulose/$BaTiO_3$ aerogel paper, and it was enormously increased to 21.25 μW cm^{-2} after coupling with a triboelectric nanogenerator (TENG).[17] Besides, cellulose-based materials show great potential for application in self-powered sensors. The environment's humidity and static or dynamic strain can be skillfully monitored and recorded.[18–21] For example, a voltage output of 1.32 V with a maximal power of 20.52 μW at 91.5% RH can be reached by using NaCl and hydroxylated multi-walled carbon nanotubes (OH-MWCNTs) as humidity-sensing electrolytes and MnO_2 and Al as electrodes.[22] A wide strain detection range (2–100%) with good repeatability (1000 times) can be achieved by assembling Cu/Al electrodes, elastic core-spun yarn coated with LiCl-carbon nanotubes (CNTs), and using latex tube encapsulation.[23]

The abovementioned studies on PENGs were all based on single-layered structures, which, in the author's opinion, is probably due to the difficulty of fabricating multilayer-structured cellulose-based films. That is because, in cellulose-based films fabricated *via* the dissolution–regeneration method, both intra- and inter-hydrogen bonds exist, which makes the films suffer the drawbacks of shrinkage during the tape-casting process. Such a phenomenon prohibits the second layer's casting on top of the first layer and makes the establishment of multilayered structures nearly impossible. This results in the loss of modulation of interfacial polarization, which is considered one of the critical factors for enhancing their figure-of-merit (FOM).[24,25] In the author's previous work, such a problem was figured out by utilizing a hydrogen bond replacement strategy. 20 wt% PVDF was blended with cellulose during the dissolution–regeneration process, and the Fourier transform infrared (FT-IR) spectra proved the formation of hydrogen bonds between the cellulose and the PVDF. Compared to pristine cellulose, a blend film has a smoother surface, and fabricating multilayered structures become possible.[12,26] Owing to this, the highest ESD ever reported for cellulose-based dielectric capacitors was obtained, further proving the significance of fabricating multilayer-structured cellulose-based films.[12] In this work, a similar strategy was employed to prepare a sandwich-structured cellulose-based PENG, denoted as CP-BCZT, in which the matrix material is a cellulose/PVDF (CP) blend film, and the $Ba_{0.7}Ca_{0.3}Zr_{0.2}Ti_{0.8}O_3$ (BCZT) ceramic powders are embedded as fillers only in the inner layer. We chose BCZT ceramic powders as fillers because they are the best lead-free candidates for highly piezoelectric lead magnesium niobite-lead titanate (PMN-PT), and the phase can be easily tuned by changing the stoichiometric ratio.[27,28] In addition, such a stoichiometric ratio is much better than those of the others, according to the results of the author's previous study.[29] Compared to traditional 0–3 structured polymer–ceramic composites, whose mechanisms of property modulation only lie in the interaction between ceramics and polymers, our work offers an extra degree of freedom in controlling the gap between adjacent particles by simply changing the inner layer thickness. By doing so, the output power of the devices can be subtly modulated, which is considered to be due to a synergistic effect between the trapped electrons and the inter-squeezing between adjacent filler particles. Based on this, their sensitivity, which is characterized as the On/Off ratio, was significantly enhanced when applied to pedometers. More importantly, such a composite film has the best mechanical properties when the fillers' concentration is 2% in volume fraction.[26] Considering the application to a pedometer, such a filler concentration will also be applied in this work. Our work proposed quite a simple way to modulate the PENGs' output performance and verified their

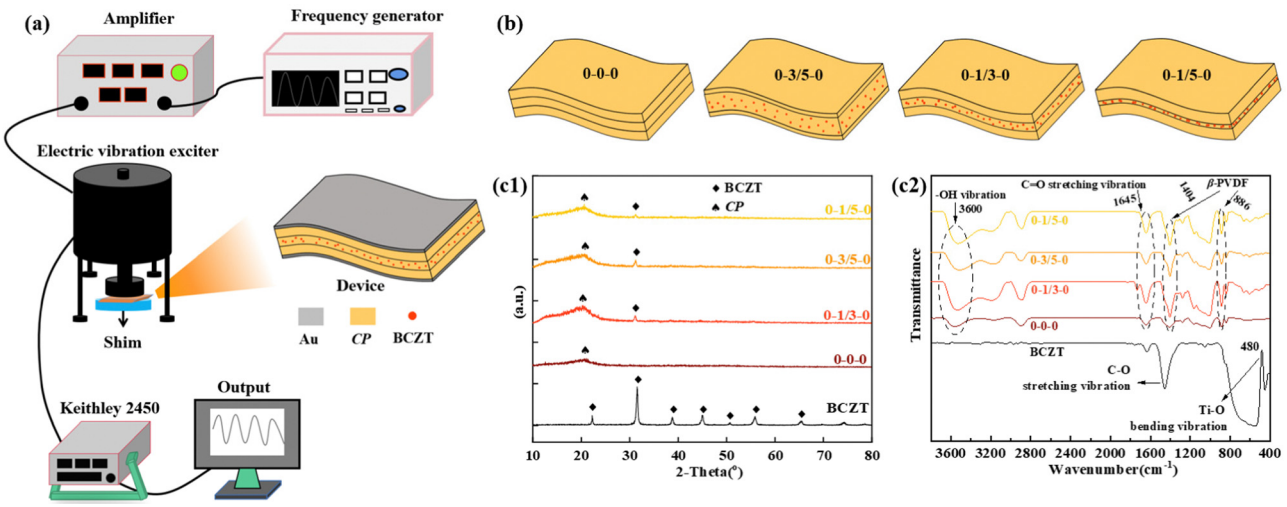

Fig. 1 (a) Sketch of measuring the output performance of PENGs; (b) sketches; (c1) XRD patterns; (c2) FT-IR spectra of the films with different configurations.

 This journal is © The Royal Society of Chemistry 2023

Published on 18 December 2023. Downloaded by Universiteit Twente on 1/16/2024 1:54:30 PM.

application in monitoring human beings' daily activity. (The Experimental section is provided in the ESI,† and the corresponding technological process is displayed in Fig. S1, ESI.†)

Fig. 1(a) briefly sketches the work process of the CP-BCZT PENG. The device is located at the bottom of an electric vibration exciter, and its output parameters can be co-adjusted by the amplifier and the frequency generator. A Keithley 2450 source meter was used for data collection, and it displays the signals on the screen. The CP-BCZT film has different configurations, but the same total thickness in this work as shown in Fig. 1(b). 0-0-0, composed of three equal-thickness sublayers, was used as a control sample without filler embedding. 0-1/3-0 has the same structure as 0-0-0 but with BCZT fillers dispersing uniformly in the inner layer. The inner layers of 0-3/5-0 and 0-1/5-0 also contain fillers, but their thickness is 3/5 and 1/5 of the total thickness, respectively. (Here, we define the structure of the pristine CP blend film without Au electrodes as the CP film, CP-BCZT without Au electrodes as the CP-BCZT film or the 0-3/5-0 film, 0-1/3-0 film, and 0-1/5-0 film. The corresponding structures with two Au electrodes are written as CP PENG and CP-BCZT PENG or 0-3/5-0 PENG, 0-1/3-0 PENG, and 0-1/5-0 PENG, respectively.) Fig. 1(c1) shows the X-ray diffraction (XRD) patterns of all the CP-BCZT films, with the pattern of BCZT fillers displayed at the bottom. The fillers exhibit a typical single-phased perovskite structure, and the broadening peak at around 21° corresponds to the peak superposition of the PVDF (110) and cellulose (200) planes.[30,31] Rietveld refinement was used to analyze BCZT's crystallographic information, and the results and parameters are shown in Fig. S2(a) and Table S1 (ESI†). A space group of *p4mm*, which belongs to the high-polarization tetragonal phase, was revealed. Diffraction signals of both the CP film and BCZT can be detected in 0-3/5-0, 0-1/3-0, and 0-1/5-0. The peaks around 886 cm^{-1} and 1404 cm^{-1} in the FT-IR spectra of films, as plotted in Fig. 1(c2), are the characteristic peaks of highly polarized β-phased PVDF.[32] Strong absorption peaks around 3600 cm^{-1}, corresponding to hydroxyl's stretching vibrations, are observed for all the films confirming the hydrogen bond network in the cellulose/PVDF matrix. However, whether the hydrogen bond replacement happens between the cellulose and the PVDF after blending PVDF is unclear; we obtained the FT-IR spectra for pristine cellulose and CP2, as shown in Fig. S2(b) (ESI†). Compared to the pristine cellulose, the absorption peak for the hydroxyl's stretching vibrations of CP shifts to a lower wave number, resulting from the formation of hydrogen bonds between F in PVDF and the hydroxyl groups in cellulose molecules. Such a peak shift agrees well with our previous work and the work of another group.[26,33] Besides, such a peak in 0-3/5-0, 0-1/3-0, and 0-1/5-0 is stronger than that in the 0-0-0 film, and it disappears in BCZT fillers, which indicates that the hydrogen bond network also exists between the fillers and the matrix; and such a network forms only during the composite process. A sharp peak at 480 cm^{-1} in the BCZT spectra, which represents

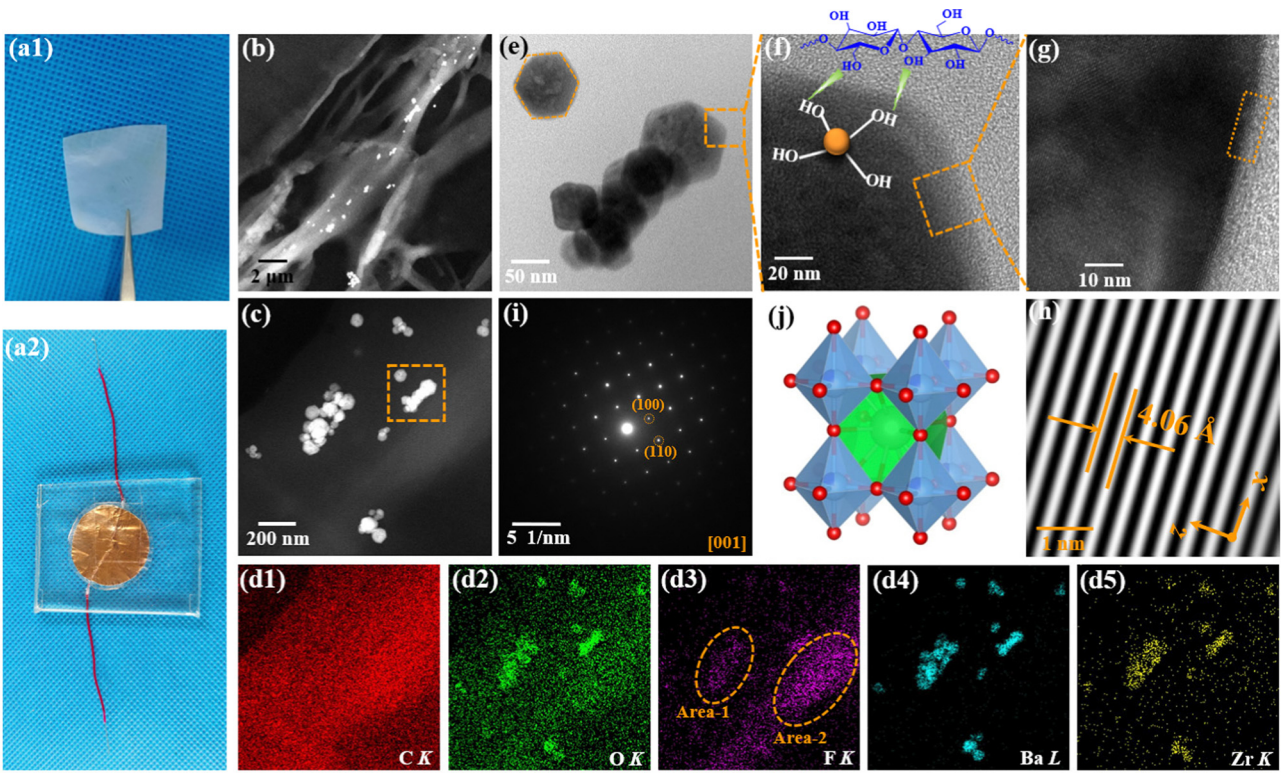

Fig. 2 Photographs of the 1/3-0-1/3 (a1) film; (a2) PENG; (b1) TEM image of a general area of the 1/3-0-1/3 film; (c) enlarged view of (b) showing the fillers' distribution; (d1)–(d5) EDS maps for C, O, F, Ba, and Zr of (b); (e) enlarged view of (b) showing the fillers' morphology; (f) enlarged view of (e) showing the interface between the filler and the matrix; (g) enlarged view of (f) showing the transient behavior of the interface between filler and matrix; (h) lattice fringes of BCZT filler; (i) EDP of single particle circled in (e); and (j) ball-stick model of the BCZT filler.

Published on 18 December 2023. Downloaded by Universiteit Twente on 1/16/2024 1:54:30 PM.

the Ti–O bending vibrations, indicates the excellent polarization of BCZT fillers, matching well with the XRD refinement results.

The cross-sectional scanning electron microscope (SEM) image of the 0-1/3-0 film with its corresponding energy-dispersive X-ray spectral (EDS) maps in Fig. S2(c1)–(c4) (ESI†) confirm its sandwiched structure. Fig. 2(a1) and (a2) show the photographs of the 0-1/3-0 film and PENGs, respectively. Transmission electron microscopy (TEM) image of a general area of the 0-1/3-0 film is displayed in Fig. 2(b), in which the cellulose fibers can be clearly distinguished, and the bright dots correspond to the fillers. Its corresponding EDS maps are provided in Fig. S3 (ESI†). Fig. 2(c) is an enlarged-viewed image of Fig. 2(b), and the EDS maps of C, O, F, Ba, and Zr are listed in Fig. 2(d1)–(d5). From Fig. 2(d1) and (d3), we can see both the cellulose and PVDF distribute uniformly in the fiber. The maps shown in Fig. 2(d2), (d4), and (d5) also agree well with the particle distribution shown in Fig. 2(c). Interestingly, two bright areas, which indicate the aggregation of F and are marked with Area-1 and Area-2 with orange dashed circles, are seen in Fig. 2(d3). Compared with Fig. 2(c), Area-1 reflects the area for BCZT particles, while Area-2 is for the CP matrix area containing no BCZT particles. Such a phenomenon shows that PVDF can aggregate both around cellulose and the CP, which might result from the hydrogen bond between PVDF and cellulose and between PVDF and BCZT particles. Fig. 2(e) is the enlarged view of the dashed area in Fig. 2(c), in which polygon BCZT particles were observed. The electron diffraction pattern (EDP) of the circled particle in Fig. 2(e) is shown in Fig. 2(i), and the single crystal character is confirmed with diffraction plane indexing. Fig. 2(f) is the enlarged view of the dashed area in Fig. 2(e), and the inserted ball-stick model explains the hydrogen bond between the cellulose fibers and the BCZT particles. The enlarged view of the dashed area in Fig. 2(f) is shown in Fig. 2(g), and the dotted area offers the intermediate state of the interface between the fillers and the matrix. Precise and smooth lattice fringes can be obtained by zooming in Fig. 2(g), and after crystal orientation calibration, the in-plane lattice parameter (a) was measured to be $\sim$4.06 Å, which fits well with the XRD refinement results. Fig. 2(h) displays the ball-stick model of the BCZT unit cell obtained by employing VESTA.[34]

The short-circuit current (I_S) of our PENGs with different configurations under an external pressure force of 10 N is illustrated in Fig. 3(a1)–(a4). As expected, the pristine CP PENG exhibits a much lower I_S than all CP-BCZT PENGs of only 0.32 μA, and interestingly, I_S of 0-1/3-0 is the highest with a value of 2.52 μA, indicating that the PENG configuration significantly affects their' output performance. Considering that the PENG's P_D is usually strongly related to the interfacial charges between the dielectric layer and the metal electrode,[35,36] we measured the devices' I–V behavior for further study. The corresponding current density–electric field (J–E) curves are plotted in Fig. S4 (ESI†). Generally, the conducting mode in dielectric devices is classified into four different modes: Schottky emission mode,

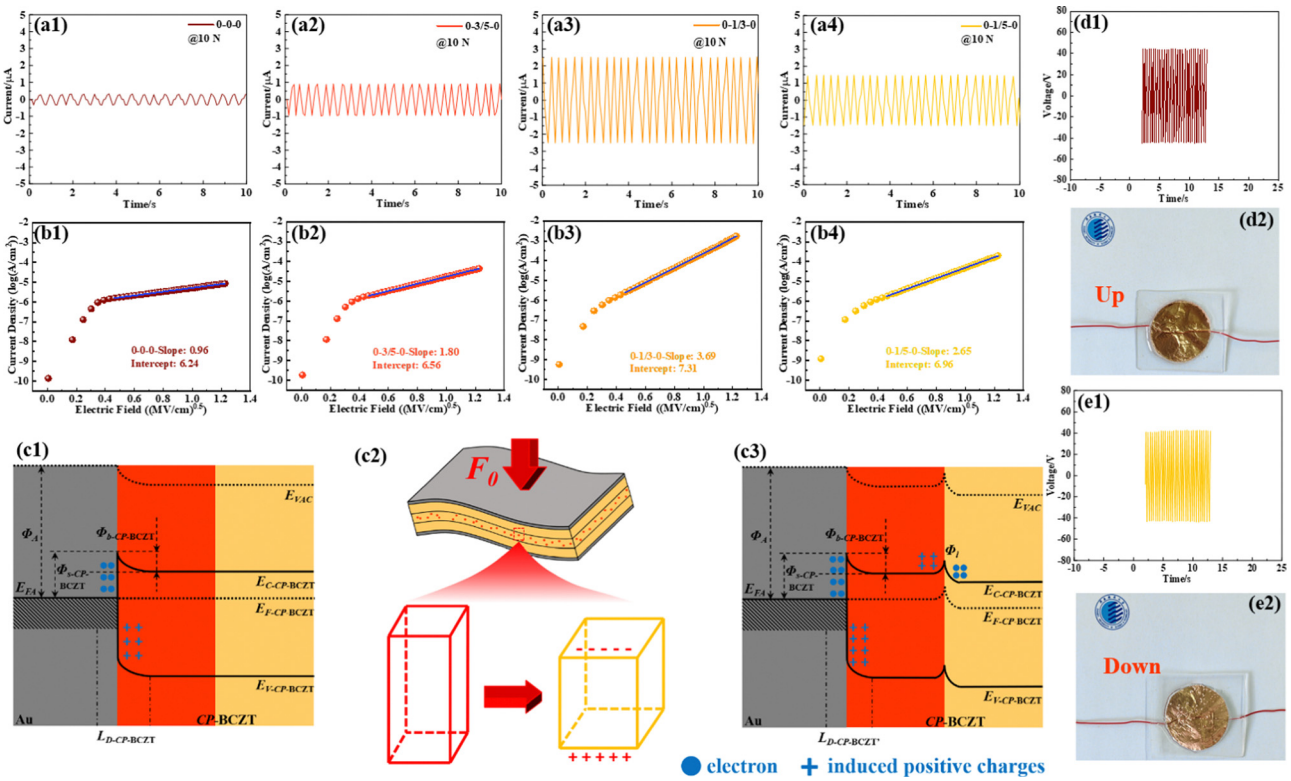

Fig. 3 (a1)–(a4) I_S; (b1)–(b4) J–E curves' fitting results of the PENGs with different configurations; (c1) band diagram of 1/3-0-1/3 PENG before F_0 applied; (c2) sketch showing the BCZT's deformation after F_0; (c3) band diagram of 1/3-0-1/3 PENG after applying F_0; (d1); (e1) V_O of the 1/3-0-1/3 PENG measured at opposite work sides and (d2); and (e2) the corresponding photos.

 This journal is © The Royal Society of Chemistry 2023

Published on 18 December 2023. Downloaded by Universiteit Twente on 1/16/2024 1:54:30 PM.

Ohmic conduction mode, space charge limited current (SCLC) mode, Poole–Frenkel (PF) mode, and Fowler–Nordheim (FN) tunneling mode.[37] After mathematical analysis, the conduction mode of our devices fits best with the Schottky emission mode because the calculated $\log J$ and $E^{0.5}$ exhibit a strictly linear relationship,[37] as depicted in Fig. 3(b1)–(b4). The interrupt value, which is related to the Schottky barrier height (Φ_s), was also calculated and inserted in each figure. Details on the expression of Schottky emission mode and the formation of Φ_s on both CP PENG and CP-BCZT PENGs are provided in the ESI.† Among the latter, 0-1/3-0 has the largest interrupt value and highest J under the same field, indicating the highest Φ_s and the largest number of electrons that overcome Φ_s under high positive voltage, respectively. This phenomenon can be explained as follows: the BCZT fillers offer more carriers than the CP matrix because of the intrinsic oxygen vacancies in the lattice, so the inner layers dominate their conducting behavior. The existence of the oxygen vacancies in the BCZT powders can be confirmed by combining X-ray photoelectron spectroscopy (XPS) and electron paramagnetic resonance (EPR) spectroscopy, as shown in Fig. S5(c1), (c2), and (d) (ESI†). Such a result agrees well with our previous conclusion.[38] When comparing 0-3/5-0 and 0-1/3-0, the inner layer of the latter has higher electron charge density and stronger interfacial interaction for its thinner thickness,[39] so more electrons can be trapped in its Au/CP interface, leading to a broader depletion layer (L_D). When comparing 0-1/3-0 and 0-1/5-0, though 0-1/5-0 has the highest electron charge density due to its thinnest inner layer thickness, the much longer distance between the fillers and the electrode results in a very high voltage drop, thus not so many electrons can be trapped in its Au/CP interface. Under this common effect, 0-1/3-0 has the highest Φ_s among the three CP-BCZT PENGs. It should also be noted here that the interrupt value of the pristine CP PENG is only 6.24, which means that it has the lowest Φ_s than CP-BCZT PENGs, which seems contradictory with the discussion in the ESI.† That is because though the majority carriers in the CP PENG and CP-BCZT PENGs are both electrons, the carriers in them have different mobilities, which affect their conducting behavior.[40] This phenomenon deserves a separate study, and we will not focus more on it. The lowest current of the CP PENG is because of its lowest electron charge density.

What we conclude now is that the 0-1/3-0 PENG has the highest Φ_s. The band diagram analysis using the J–E curves was based on the simplification of assuming an equivalent band structure in the CP-BCZT films. As for discussing the output performance, such an assumption becomes invalid because electron transport is no longer caused by external voltage. The band diagram of CP-BCZT PENGs under zero voltage or force is shown in Fig. 3(c1). When an external pressure force (F_0) is applied on the device, the BCZT filler, which was proved to be in the tetragonal phase as abovementioned, suffers a deformation with the c axis shrinking and the a axis elongating, as sketched in Fig. 3(c2). Then, a piezometric potential forms on the opposite surfaces of the unit cell and induces an equal amount of different charges in the BCZT/CP interface. Because the electron affinity of BCZT is higher than that of CP (see ESI†), the generated electrons can hardly overcome the interfacial barrier (Φ_i), and more and more electrons thus aggregate in the BCZT/CP interface with increasing external force, as depicted in Fig. 3(c3). This phenomenon can be regarded as due to applying a reverse bias to the device,[41,42] resulting in a decrement of the build-in potential ($\Phi_{b\text{-}CP\text{-}BCZT}$) and electrons' de-trapping. Such a de-trapping behavior is thought to be the primary reason for generating I_S, and now the reason for the 0-1/3-0 PENG's best output performance seems revealed: due to the highest number of trapped electrons, more can be released from 0-1/3-0 than the others when under the same force. We should also notice that such a conclusion is based on the assumption that BCZT generates the same charges, and actually, due to the inter-squeezing effect, 0-1/5-0 generates the most charges, and then 0-1/3-0, and 0-3/5-0 generate the least, as we deduced in the ESI.† Also, because of the longer distance between the fillers and the electrode in the 0-1/5-0 PENG, a significant part of generated electrons is lost during the transporting. Due to this synergistic effect, the 0-1/3-0 PENG exhibits the highest I_S among all. In other words, by simply changing the inner layer thickness, the output performance of the PENG can be modulated by regarding the BCZT filler as a trigger. Fig. 3(d1) and (e1) show the output voltage (V_O) of 0-1/3-0 with opposite work sides under 10 N with the photographs displayed in Fig. 3(d2) and (e2), respectively. As expected, no difference in output performance can be detected, indicating the non-oriented characteristic of our device.

The frequency dependence of the dielectric constant (ε) and dielectric loss ($\tan\delta$) of all the devices is plotted in Fig. 4(a) with the corresponding ε–T and $\tan\delta$–f curves plotted in Fig. S7 (ESI†). ε decreases with increasing f for all the devices, which is typical for dielectric materials. The most trapped electrons in 0-1/3-0 result in its highest ε and $\tan\delta$ in the low f range for the polarization caused by the trapped electrons failing to keep up with the electric field switching. Because of this, much polarization can be triggered in the polarization–electric field (P–E) measurement, as illustrated in Fig. 4(b), with the P–E loops under different electric fields shown in Fig. S8 (ESI†). The pristine CP PENG shows a typical linear polarization behavior. Fig. 4(c1) and (c2) show the 0-1/3-0's open-circuit voltage (V_O) and I_S under different external pressure forces at 4 Hz. Both V_O and I_S increase with increasing force from 2 N to 10 N. Further force enhancement affects its output performance little for the threshold of piezoelectric potential has already been reached, and finally, a P_D of $\sim$4.28 μW cm^{-2} was obtained. 0-1/3-0's output performance at 10 N but different vibration frequencies (f_V) is shown in Fig. 4(d1) and (d2). Because of the viscoelasticity of cellulose, both the V_O and I_S of the PENG increase with increasing f_V from 1 Hz to 4 Hz, resulting in an increase of P_D from $\sim$0.17 μW cm^{-2} to $\sim$4.28 μW cm^{-2} with an increment of as high as 25 times.[43,44] Besides, the increasing rate of charge exchange with increasing f_V has the same effect on this phenomenon,[45] and further f_V increase shows no contribution to improving its P_D. Fig. 4(e) displays the I_S of the 0-1/3-0 PENG during a long-term use of 3 min. Almost no decrement of I_S can

Published on 18 December 2023. Downloaded by Universiteit Twente on 1/16/2024 1:54:30 PM.

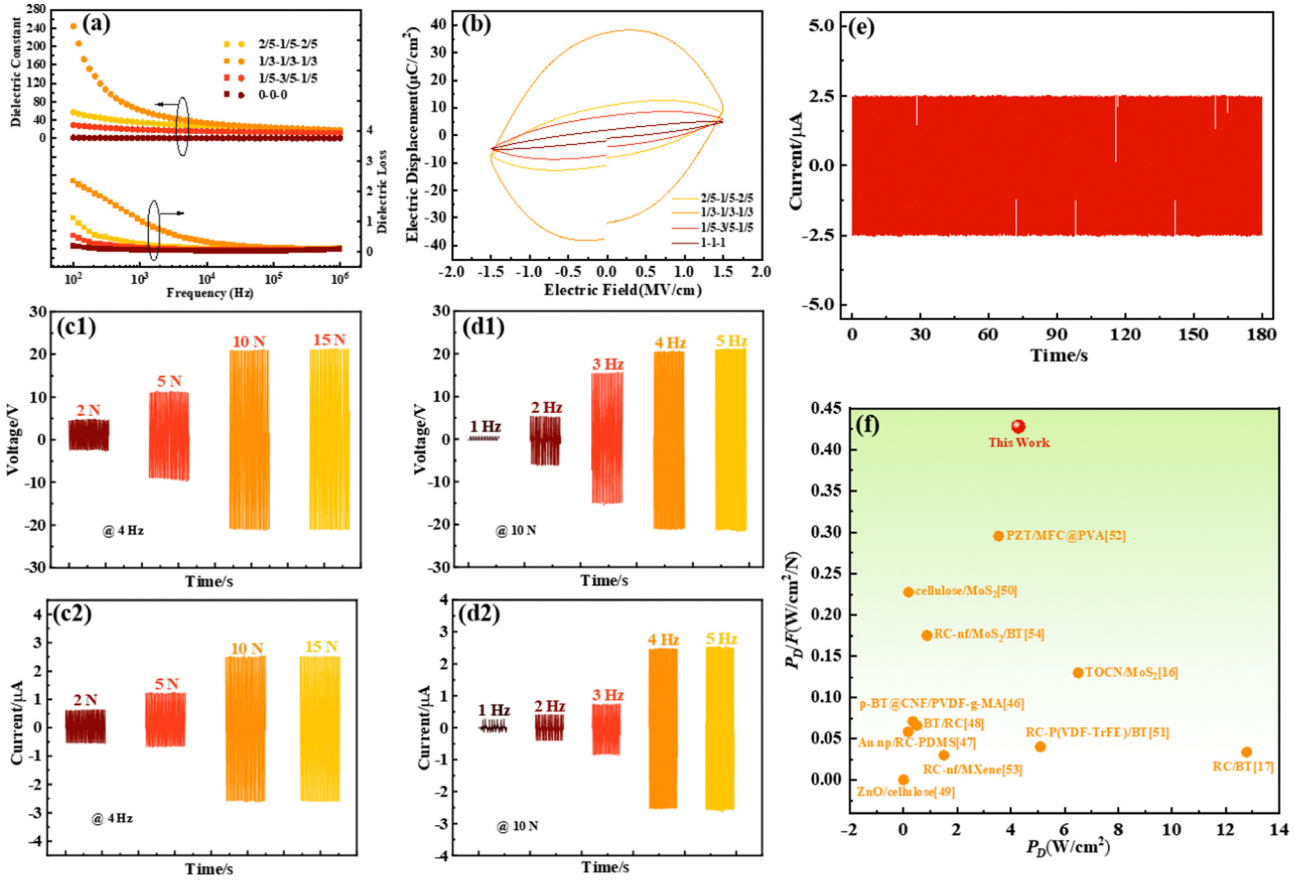

Fig. 4 (a) The frequency dependence of dielectric constant (ε) and dielectric loss (tan δ); (b) P–E loops of the PENGs with different configurations; (c1) V_O and (c2) I_S of the 1/3-0-1/3 PENG measured at different external pressure forces under 4 Hz; (d1) V_O and (d2) I_S of the 1/3-0-1/3 PENG measured under different frequencies at 10 N; (e) long-term output performance of the 1/3-0-1/3 PENG; and (f) the comparison of the output performance between the 1/3-0-1/3 PENG and some typical cellulose-based PENGs.

be detected during such a process, demonstrating its reliability. In addition to P_D, as an environmentally friendly device, energy consumption should also be considered. Fig. 4(f) compares the output performance of the 0-1/3-0 PENG in our work and some other typical cellulose-based PENGs, with the X-axis and Y-axis as the P_D and the P_D triggered by unit force (P_D/F), respectively.[16,17,46–54] Though the P_D of the 0-1/3-0 PENG does not have much advantage over the other devices, the P_D/F is the highest among all the devices. It means that more converted electric energy can be output in our device when consuming the same amount of mechanical energy, and further study should focus on improving the P_D threshold.

Step recording is one of the most important parameters in health monitoring, and after COVID-19, more and more people are paying their attention to this. When people are walking, the tiptoe and the heel generally suffer different forces from the ground. When we put a PENG under different positions of the sole, as we display in Fig. 5(a1) and (a2), the output performance is different, though such a difference can sometimes be very weak. Fig. S9 (ESI†) shows the generated I_S of different PENGs when put in different positions of the sole, and such signals have both positive and negative currents. Suppose an external rectifier circuit is embedded, as sketched in Fig. 5(b), in this case, the signals in Fig. S9 (ESI†) can be converted to unidirectional, as shown in Fig. 5(c1)–(c4), in which the higher current signal is written as On and the lower one as Off. As mentioned above, due to the synergistic effect between the trapped electrons and the inter-squeezing between adjacent particles, the strongest tiptoe and heel current signal is observed for 1/3-0-1/3. The precision of a pedometer relies on the current difference between the tiptoe and the heel, which can be defined as the On/Off ratio, and such a ratio variation of all the PENGs is plotted in Fig. 5(d). Obviously, the 1/3-0 PENG shows the highest precision. In practical application, different harsh environments should be considered. Fig. 5(d1)–(d4) display the water contact angle test for all the CP-BCZT films, and compared to 0-0-0, films with BCZT fillers exhibit a much lower water contact angle, indicating inferior water resistance behavior, and such a behavior between 0-3/5-0, 0-1/3-0, and 0-1/5-0 shows little difference. Revealing the factors affecting the water contact angle in our films deserves a separate work, and as this is a communication article, we would not like to give a further discussion here. However, based on previous literature, such a difference is mainly attributed to the micro-holes in the interface between the water and film surface, and also attributed to the thickness, density, and roughness.[55–57] Though the CP-

 This journal is © The Royal Society of Chemistry 2023

Published on 18 December 2023. Downloaded by Universiteit Twente on 1/16/2024 1:54:30 PM.

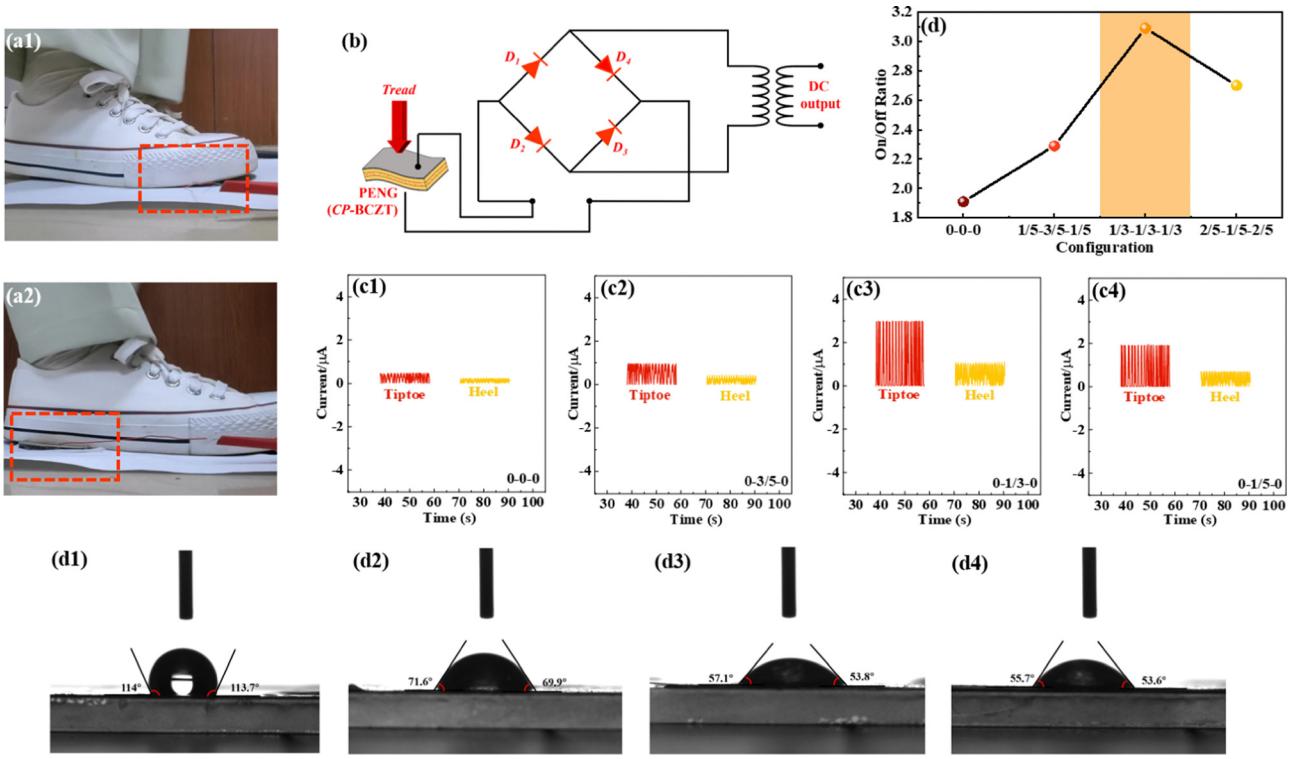

Fig. 5 (a1) and (a2) Photograph showing the 1/3-0-1/3 PENG under different positions of the sole; (b) a typical external rectifier circuit that can filter the I_S negative signal; (c1)–(c4) the filtered I_S of the PENGs with different configurations when put in different positions of the sole I_S of the PENGs with different configurations; and (d) the calculated ON/OFF ratio from (c1)–(c4); (d1)–(d4) the water contact angle of the films with different configurations.

BCZT films show smaller angles than the pristine CP films, their hydrophobicity is still good, which reveals that they have the potential to be used in wet circumstances and even in rainy weather.

Conclusion

Using a hydrogen bond replacement strategy, biomass-based multilayer structured PENGs were fabricated in which the matrix is a cellulose/PVDF blend film, and the fillers are BCZT ceramic powders. The complex hydrogen bond network, confirmed by combining multiple characterization methods, enables the uniform distribution of fillers in the inner layer. By changing the inner layer thickness, the output performance of the PENGs can be subtly modulated, which is proved to be attributed to the synergistic effect between the trapped electrons and the inter-squeezing between adjacent particles. A device with a configuration of 1/3-0-1/3 exhibits a P_D of $\sim$4.28 μW cm^{-2}, and its P_D/F, which is defined as P_D triggered by unit force, is the highest among those of most of the current cellulose-based PENGs, indicating its low energy consumption character. Besides, when applying to a pedometer, it shows high sensitivity and great potential for working in humid environments.

Author contributions

Zixiong Sun: conceptualization, methodology, writing – reviewing and editing, supervision, and funding acquisition. Siting Wang: data curation and formal analysis. Shibo Zhao: formal analysis. Hansong Wei: formal analysis. Guodong Shen: writing – reviewing and editing. Yongping Pu: writing – reviewing and editing. Sufeng Zhang: funding acquisition and supervision.

Conflicts of interest

The authors declared that they have no conflicts of interest in this work.

Acknowledgements

This work was financed by the National Natural Science Foundation of China (52002234, 22078187), the International Joint Research Center for Biomass Chemistry and Materials, Shaanxi International Science and Technology Cooperation Base (2018GHJD-19), Shaanxi Key Industry Innovation Chain Projects (2020ZDLGY11-03), China-CEEC University Joint Education Project (2021099), the Open Foundation of Key Laboratory of Auxiliary Chemistry and Technology for Chemical Industry, Ministry of Education, Shaanxi University of Science and Technology (No. KFKT2021-09), and Shaanxi Collaborative Innovation Center of Industrial Auxiliary Chemistry and Technology, Shaanxi University of Science and Technology (No. KFKT2021-09).

Published on 18 December 2023. Downloaded by Universiteit Twente on 1/16/2024 1:54:30 PM.

References

1 P. K. Annamalai, A. K. Nanjundan, D. P. Dubal and J. B. Baek, *Adv. Mater. Technol.*, 2021, **6**, 2001164.
2 M. Zhang, H. Du, K. Liu, S. Nie, T. Xu, X. Zhang and C. Si, *Adv. Compos. Hybrid Mater.*, 2021, **4**, 865.
3 Y. Song, Z. Shi, G. H. Hu, C. Xiong, A. Isogai and Q. Yang, *J. Mater. Chem. A*, 2021, **9**, 1910.
4 M. Li, Y. Jie, L. H. Shao, Y. Guo, X. Cao, N. Wang and Z. L. Wang, *Nano Res.*, 2019, **12**, 1831–1835.
5 Z. Sun, Z. Wang, Y. Tian, G. Wang, W. Wang, M. Yang, X. Wang, F. Zhang and Y. Pu, *Adv. Electron. Mater.*, 2020, **6**, 1900698.
6 Z. Sun, Y. Bai, J. Liu, G. Jian, C. Guo, L. Zhang and Y. Pu, *J. Alloys Compd.*, 2022, **909**, 164735.
7 Y. Yin, J. He, C. Zhang, J. Chen, J. Wu, Z. Shi, C. Xiong and Q. Yang, *Cellulose*, 2021, **28**, 1541–1553.
8 C. Zhang, Y. Yin, Q. Yang, Z. Shi, G. Hu and C. Xiong, *ACS Sustainable Chem. Eng.*, 2019, **7**, 10641–10648.
9 X. Zheng, Y. Yin, P. Wang, C. Sun, Q. Yang, Z. Shi and C. Xiong, *Int. J. Biol. Macromol.*, 2023, 125220.
10 Y. Yin, C. Zhang, W. Yu, G. Kang, Q. Yang, Z. Shi and C. Xiong, *Energy Storage Mater.*, 2020, **26**, 105–111.
11 L. Wu, J. Zhao, Z. Li, Y. Zhai, Y. Zhang, Q. Zhen, Y. Cheng, X. Ding, P. Li and J. Liu, *J. Mater. Chem. C*, 2022, **10**, 15416–15423.
12 Z. Sun, J. Liu, H. Wei, Q. Guo, Y. Bai, S. Zhao, S. Wang, L. Li, Y. Zhang and Y. Tian, *J. Mater. Chem. A*, 2023, **11**, 20089.
13 Z. Sun, H. Wei, S. Zhao, Q. Guo, Y. Bai, S. Wang, P. Sun, K. Du, Y. Ning, Y. Tian, X. Zhang, H. Jing, Y. Pu and S. Feng, *J. Mater. Chem. A*, 2024, **12**, 128–143.
14 G. Zhang, Q. Liao, M. Ma, F. Gao, Z. Zhang, Z. Kang and Y. Zhang, *Nano Energy*, 2018, **52**, 501–509.
15 T. Wu, Y. Song, Z. Shi, D. Liu, S. Chen, C. Xiong and Q. Yang, *Nano Energy*, 2021, **80**, 105541.
16 Y. Song, T. Wu, J. Bao, M. Xu, Q. Yang, L. Zhu and C. Xiong, *Carbohydr. Polym.*, 2022, **288**, 119407.
17 K. Shi, X. Huang, B. Sun, Z. Wu, J. He and P. Jiang, *Nano Energy*, 2019, **57**, 450–458.
18 Z. Duan, Y. Jiang, Q. Huang, Z. Yuan, Q. Zhao, S. Wang and H. Tai, *J. Mater. Chem. C*, 2021, **9**, 13659–13667.
19 Z. Duan, Z. Yuan, Y. Jiang, Y. Liu and H. Tai, *J. Mater. Chem. C*, 2023, **11**, 5585–5600.
20 Z. Duan, Y. Jiang, Q. Huang, S. Wang, Q. Zhao, Y. Zhang and H. Tai, *Cellulose*, 2021, **28**, 6389–6402.
21 Z. Duan, Y. Jiang, Q. Huang, S. Wang, Y. Wang, H. Pan and H. Tai, *Smart Mater. Struct.*, 2021, **30**, 055012.
22 M. Zhang, Z. Duan, B. Zhang, Z. Yuan, Q. Zhao, Y. Jiang and H. Tai, *Nano Energy*, 2023, **15**, 108745.
23 Q. Huang, Y. Jiang, Z. Duan, Y. Wu, Z. Yuan, M. Zhang and H. Tai, *Nano Energy*, 2023, **118**, 108997.
24 X. Zhang, J. Feng, X. Liu and J. Zhu, *Carbohydr. Polym.*, 2012, **89**(1), 67–71.
25 H. Tu, M. Zhu, B. Duan and L. Zhang, *Adv. Mater.*, 2021, **33**(28), 2000682.
26 S. Zhang, J. Liu, Q. Guo, N. Wei, Y. Ning, Y. Bai and Y. Pu, *Composites, Part A*, 2023, **165**, 107329.
27 W. Liu and X. Ren, *Phys. Rev. Lett.*, 2009, **103**, 257602.
28 Z. Sun, C. Ma, M. Liu, J. Cui, L. Lu, J. Lu and C. L. Jia, *Adv. Mater.*, 2017, **29**, 1604427.
29 Large Energy Density, Excellent Thermal Stability, and High Cycling Endurance of Lead-Free $BaZr_{0.2}Ti_{0.8}O_3$ Film Capacitors.
30 J. Gong, J. Li, J. Xu, Z. Xiang and L. Mo, *RSC Adv.*, 2017, **7**(53), 33486–33493.
31 K. S. Tan, W. C. Gan, T. S. Velayutham and W. H. Abd Majid, *Smart Mater. Struct.*, 2014, **23**(12), 125006.
32 W. Chen, H. He, H. Zhu, M. Cheng, Y. Li and S. Wang, *Polymers*, 2018, **10**, 592.
33 P. Wang, Y. Yin, L. Fang, J. He, Y. Wang, H. Cai and C. Xiong, *Composites, Part A*, 2023, **164**, 107325.
34 K. Momma and F. Izumi, *J. Appl. Crystallogr.*, 2011, **44**, 1272–1276.
35 R. Hinchet, S. Lee, G. Ardila, L. Montès, M. Mouis and Z. L. Wang, *Adv. Funct. Mater.*, 2014, **24**(7), 971–977.
36 X. Yang and W. A. Daoud, *Adv. Funct. Mater.*, 2016, **26**(45), 8194–8201.
37 F. C. Chiu, *Adv. Mater. Sci. Eng.*, 2014, 578168.
38 Z. Sun, S. Huang, W. Zhu, Y. A. Birkhölzer, X. Gao, R. A. Avila, H. Huang, X. Lou, E. P. Houwman, M. D. Nguyen, G. Koster and G. Rijnders, *APL Mater.*, 2023, **11**, 101129.
39 A. A. Narasimulu, P. Zhao, N. Soin, K. Prashanthi, P. Ding, J. Chen and J. Luo, *Nano Energy*, 2017, **40**, 471–480.
40 A. Bolognesi, A. Di Carlo and P. Lugli, *Appl. Phys. Lett.*, 2002, **81**(24), 4646–4648.
41 L. Zhao, H. Li, J. Meng, Y. Zhang, H. Feng, Y. Wu and Z. Li, *Sci. Bull.*, 2021, **66**(14), 1409–1418.
42 J. Meng, H. Li, L. Zhao, J. Lu, C. Pan, Y. Zhang and Z. Li, *Nano Lett.*, 2020, **20**(7), 4968–4974.
43 U. Erturun, A. A. Eisape, S. H. Kang and J. E. West, *Appl. Phys. Lett.*, 2021, **118**, 6.
44 Y. Qin, W. Zhang, Y. Liu, J. Zhao, J. Yuan, M. Chi and S. Nie, *Nano Energy*, 2022, 108079.
45 S. Hajra, Y. Oh, M. Sahu, K. Lee, H. G. Kim, B. K. Panigrahi and H. J. Kim, *Sustainable Energy Fuels*, 2021, **5**(23), 6049–6058.
46 L. Wang, T. Cheng, W. Lian, M. Zhang, B. Lu, B. Dang, K. Tan, C. Liu and C. Shen, ''Flexible layered cotton cellulose-based nanofibrous membranes for piezoelectric energy harvesting and self-powered sensing'', *Carbohydr. Polym.*, 2021, **275**, 118740.
47 M. Pusty and P. M. Shirage, ''Gold nanoparticle-cellulose/PDMS nanocomposite: a flexible dielectric material for harvesting mechanical energy'', *RSC Adv.*, 2020, **10**(17), 10097–10112.
48 H. Y. Choi and Y. G. Jeong, ''Microstructures and piezoelectric performance of eco-friendly composite films based on nanocellulose and barium titanate nanoparticle'', *Composites, Part B*, 2019, **168**, 58–65.
49 M. Manikandan, P. Rajagopalan, N. Patra, S. Jayachandran, M. Muralidharan, S. S. Prabu, I. A. Palani and V. Singh,

 This journal is © The Royal Society of Chemistry 2023

Published on 18 December 2023. Downloaded by Universiteit Twente on 1/16/2024 1:54:30 PM.

''Development of Sn-doped ZnO based ecofriendly piezoelectric nanogenerator for energy harvesting application'', *Nanotechnology*, 2020, **31**(18), 185401.

50 S. Chen, J. Li, Y. Song, Q. Yang, Z. Shi and C. Xiong, ''Flexible and environment-friendly regenerated cellulose/MoS2 nanosheet nanogenerators with high piezoelectricity and output performance'', *Cellulose*, 2021, **28**(10), 6513–6522.

51 H. Zhang, C. K. Jeong, Z. Shen, J. Wang, H. Sun, Z. Jian, W. Chen and Y. Zhang, ''Ultrahigh augmentation of flexible composite-based piezoelectric energy harvesting efficiency via polymer-impregnated nanoparticles network within 3D cellulose scaffold'', *Composites, Part B*, 2022, **236**, 109813.

52 Y. Guo, M. Bai, Q. Wang, L. Liu, S. Yu, B. Kong, F. Lv, M. Guo, L. Li, L. Zhang, Y. Lin and W. Li, ''A self-powered wearable piezoelectric nanogenerator for physiological monitoring based on lead zirconate titanate/microfibrillated cellulose@polyvinyl alcohol (PZT/MFC@PVA) composition'', *Chem. Eng. J.*, 2023, **460**, 141598.

53 Y. Zong, R. Wang, S. Xu, R. Zhang and Z. Zhang, ''Flexible Piezoelectric Nanogenerator Based on Cellulose Nanofibril/MXene Composite Aerogels for Low-Frequency Energy Harvesting'', *ACS Appl. Nano Mater.*, 2023, **6**(10), 9021–9031.

54 M. Xu, T. Wu, Y. Song, M. Jiang, Z. Shi, C. Xiong and Q. Yang, ''Achieving high-performance energy harvesting and self-powered sensing in a flexible cellulose nanofibril/MoS_2/$BaTiO_3$ composite piezoelectric nanogenerator'', *J. Mater. Chem. C*, 2021, **9**(43), 15552–15565.

55 S. Rbihi, A. Aboulouard, L. Laallam and A. Jouaiti, *Surf. Interfaces*, 2020, **21**, 100708.

56 G. Rodionova, Ø. Eriksen and Ø. Gregersen, *Cellulose*, 2012, **19**, 1115–1123.

57 Z. Tang, H. Li, D. W. Hess and V. Breedveld, *Cellulose*, 2016, **23**, 1401–1413.